**Showcasing research from the research teams of Pedro Reis (Elasticity, Geometry and Statistics Laboratory, Massachusetts Institute of Technology) and Ashkan Vaziri (High Performance Materials and Structures Laboratory, Northeastern University).**

Title: Localization of deformation in thin shells under indentation

Sharp regions of localized deformation emerge in thin shells under indentation. The onset and evolution of these structures depends strongly on the shape of the indentor, which modifies the geometry and mechanics of contact, thereby markedly affecting the mechanical response.
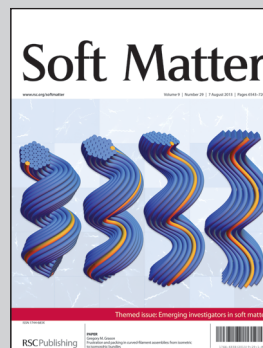
RSC Publishing

Localization of deformation in thin shells under indentation

Alice Nasto,[a] Amin Ajdari,[c] Arnaud Lazarus,[a] Ashkan Vaziri[c] and Pedro M. Reis*[ab]

We perform a hybrid experimental and numerical study of the localization of deformation in thin spherical elastic shells under indentation. Past a critical indentation, the deformation of the shell ceases to be axisymmetric and sharp points of localized curvature form. In plates, these sharp points are known as d-cones. By way of analogy, we refer to regions of localization in shells as *s-cones*, for 'shell-cones'. We quantify how the formation and evolution of s-cones is affected by the indenter's curvature. Juxtaposing results from precision model experiments and finite element simulations enables us to explore the frictional nature of the shell–indenter contact and characterize the relative properties of strain energy focusing, at different loci of localization. Our combined experimental and computational approach allows us to gain invaluable physical insight towards rationalizing this geometrically nonlinear process.

Introduction

Localization in thin shells is observed over a large range of length scales; from colloidal capsules at the microscale[1] to aircraft[2,3] and architectural domes.[4,5] When localization is induced by indentation, the shape of the indenter affects the nature of the indenter–shell contact. This is an important consideration in applications such as Atomic Force Microscopy (AFM),[6] which has been used to measure the mechanical response of shell structures such as microcapsules[7] and bacteria.[8] The curvature of the AFM tip relative to the curvature of the object that it indents is often non-negligible. As such, the relationship between the mechanical response and the nature of the indenter–object contact is critical for understanding the process.

The mechanics of shells is inextricably connected to its geometry[9] and, for a shell with positive Gaussian curvature, bending and stretching are coupled. Stretching is energetically costly and the deformation of a shell is governed in large part by a need to minimize stretching, in favor of bending, to preserve the isometry of the surface (*i.e.* preserving the distance along the surface between any two points). A shell is curved in its undeformed shape, yet when it undergoes large deformations, the indented surface can develop sharp angular shapes. Energy localizes at these vertices and along straight edges, which, although locally costly, minimize stretching globally.[10] In the

linear regime, there have been a number of attempts to rationalize the interplay between geometry and mechanics, ranging from the seminal work of Reissner[11] on spherical shells to the more recent study of geometry-induced rigidity in non-spherical pressurized shells.[12] There has been much less attention, however, on localization in shells under large deformations for which a general predictive framework is still aloof.

The scenario for large deformations in doubly curved shells is not unlike what is observed in plates and other developable surfaces (*e.g.* cylindrical shells) under large deformations, where energy localizes along *ridges* and vertices, known as *d-cones* for 'developable cones'.[13–17] These localized structures have been well studied and characterized through experimental, numerical, and theoretical work. Drawing an analogy with d-cones in plates and cylindrical shells,[17] we denote the localized objects in doubly curved shells by *s-cones*, for 'shell cones', highlighting that they are not developable. Previous studies on large deformations and localization in shells have considered a variety of loading mechanisms. Some studies induce large deformations in shells through depressurization and characterize a variety of buckled shapes.[18–20] In other studies, shells are deformed by indentation, with the most common scenarios involving indentation by either a point load[10,21–23] or a plate load.[21,23–29]

Here, we fill the gap between point and plate indentation by studying indenters with intermediate curvatures. We are motivated by the fact that natural and engineering instances of indentation often occur in this intermediate range. Our goal is to develop insight and gain a better understanding on the relationship between the geometry of the shell, the shape of the indenter, and the mechanics of the localization process in the nonlinear regime of shells under indentation. Towards this

[a]*Department of Mechanical Engineering, Massachusetts Institute of Technology (MIT), 77 Massachusetts Av., Cambridge, MA, USA. E-mail: preis@mit.edu*

[b]*Department of Civil & Environmental Engineering, MIT, Cambridge, MA, USA*

[c]*Department of Mechanical and Industrial Engineering, Northeastern University, Boston, MA, USA*

end, we perform precision model experiments using hemispherical elastomeric shells and indenters with custom controlled geometries that we custom fabricate using rapid prototyping. The shells are made using a coating technique (Fig. 1a) whereby the surface of a mold (Fig. 1b) is coated by a liquid polymer, which eventually cures, resulting in a thin shell with uniform thickness (Fig. 1c). Our shells have radius $R_2 = 25$ mm and thickness $t = 0.280 \pm 0.027$ mm. More details on the shell and indenter fabrication are given in the Materials and methods section.

Our indenters have a range of radii of curvature, such that the ratio between the radius of the indenter, R_1, and that of the shell, R_2, defined as $\Gamma = R_1/R_2$ (shown schematically in Fig. 1d), lies in the full range $0 < \Gamma < \infty$, from point load to plate load, respectively (examples given in Fig. 1e). The mechanical response is quantified through indentation tests and the evolution of the deformation of the shell is captured with digital images using a camera located underneath the shell. In parallel, we perform Finite Element Analysis (FEA) of the same scenario explored experimentally, finding excellent quantitative agreement between the two. Given the predictive power of our numerics, we then exploit the simulations to gain further insight into quantities that cannot be readily accessed experimentally, such as the role of friction in the mechanical response and characterization of localization of the strain energy. We find that patterns of localization are reproducible with all values of Γ, in both experiments and simulations, and show that the indenter's shape affects both the number of s-cones that form as well as the indentation onset for localization. The mechanical response is also significantly affected by the nature of the shell–indenter contact and important qualitative differences are observed between sharp indenters ($\Gamma < 1$) and blunt indenters ($\Gamma > 1$).
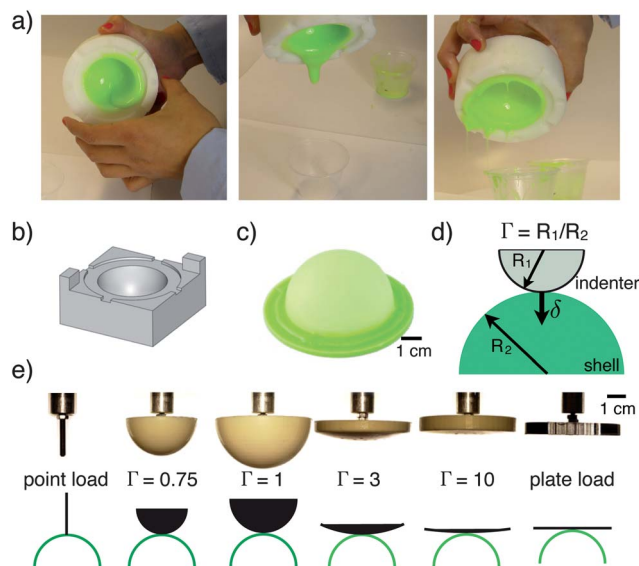
Point indentation

We start by considering the case of point indentation. A thin hemispherical shell is clamped at its equator. A point load is then applied to the shell's pole along its axis and the indentation is performed quasi-statically at 5 mm.min^{-1} (see Materials and methods for more details). This scenario is implemented and studied experimentally and through FEA simulations. In the experiments, the evolution of the deformation upon indentation is captured through digital imaging, as shown in the sequence of photographs in Fig. 2a. The white lines in the photographs, which aid identifying the loci of localization, correspond to light reflections from the ridge-like regions, where the shell inverts. The FEA simulations provides additional means to quantify the localization process, for example by having access to the energy density as indicated by the color map in Fig. 2b. Localized structures are associated with sharp increases in energy density.

In Fig. 2a and b, we present a sequence of representative snapshots of the shell at different stages of indentation, for the experiments and the FEA simulations, respectively, at the same values of the control parameters. Excellent qualitative and quantitative agreement is found between the two. We define the
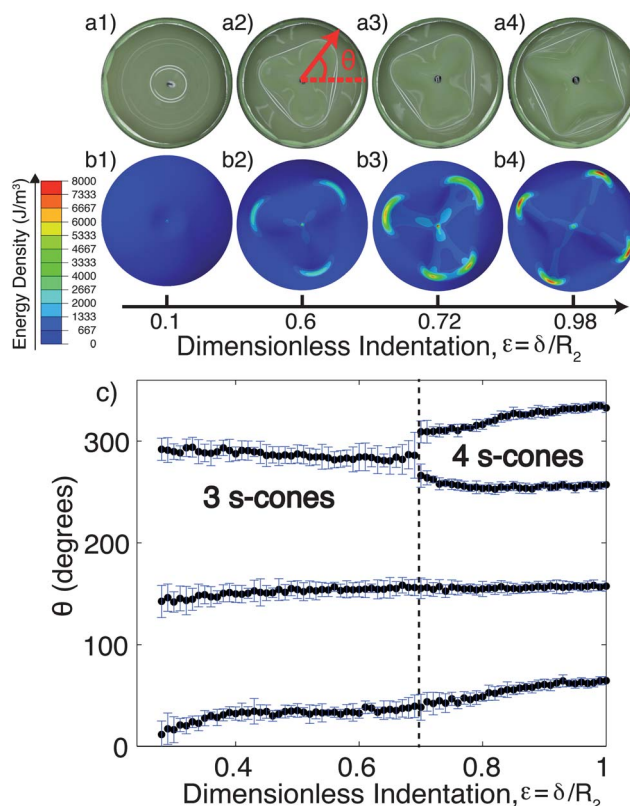

Fig. 1 Experimental setup. (a) Coating technique used to fabricate thin and uniform hemispherical shells. (b) CAD model of indenter and shell molds. (c) Hemispherical elastomeric shell created by the coating technique. (d) Schematic of indenter, with radius R_1 and shell, with radius R_2. (e) Series of indenters ranging from $\Gamma = R_1/R_2 = 0$ (point load) to $\Gamma = \infty$ (plate load).

Fig. 2 Point indentation. (a) Experimental snapshots (captured from underneath the shell) of the evolution of the pattern of localization for an elastomeric shell under point indentation at the pole. The white reflection corresponds to the location at which the shell inverts. (b) Snapshots from FEA simulations of an elastomeric shell under point indentation at the pole. (c) Angular position of s-cones vs. indentation obtained from experimental images. θ is defined as in the red schematic drawn in (a2).

dimensionless indentation as $\varepsilon = \delta/R_2$, where δ is the indentation displacement and R_2 is the radius of the shell. At small values ε, the cap of the shell inverts inwards, forming an axisymmetric circular ridge, known as Pogorelov ridge,[30] along which the shell stretches (Fig. 2a1 and b1). Due to the high energetic cost associated with stretching, past a critical value of indentation, the round ridge loses its axisymmetry and strain focuses at three conical-like vertices, the *s-cones*, which help reducing the stretching globally (Fig. 2a2 and b2).[21] Once these three s-cones form, the inverted portion of the shell develops a tetrahedral shape. One vertex of the tetrahedron is located at the point where the indenter makes contact with the shell. The outer three vertices are located along a path on the surface where the shell inverts. These three s-cones are connected by straight segments, denoted by *ridges*, which act as folds between the mostly undeformed outer shell and the inner inverted region. Inside the inverted tetrahedral region, additional folds form, which we refer to as *gullies*, that connect each of the s-cones to the point of indentation. As the shell is indented further, the s-cones travel along the shell's surface and eventually new s-cones can form. It is interesting to note that the birth of additional s-cones appears by division of an existing localized structure (Fig. 2a3 and b3), rather than nucleation at a previously smooth region of the shell. Further indentation past the splitting event results in four well defined s-cones (Fig. 2a4 and b4).

To further quantify the process of birth and growth of s-cones, we perform digital image processing on the experimental frames to track the angular position of each of the s-cones (projected on a plane perpendicular to the vertical axis of indentation). The schematic definition of the s-cone's angular position, θ, is presented in Fig. 2a2. As the shell is indented, the evolution of the s-cones' angular position illustrates the splitting mechanism by which new s-cones form; at $\varepsilon \sim 0.7$, the forth new s-cone emerges through the branching of one of the older three.

Localization of energy for point indentation

We proceed by further characterizing the various localized structures identified above for point load, using quantities extracted from the FEA that are not available experimentally. We shall later demonstrate the power of our FEA simulations in predictively reproducing the experimental results. In particular, our focus now goes to a quantitative comparison of the strain energy density, the energy stored in a body due to deformation per unit volume, for the *s-cones*, *ridges*, and *gullies*. We analyze the specific example of indentation to $\delta = 15$ mm ($\varepsilon = 0.6$). The paths along the shell's surface that we shall use in our discussion are schematically drawn on top of the FEA snapshots shown in Fig. 3a and b.

In Fig. 3c, we trace the energy density along Path #1, which is a closed contour that traverses over the range of the three s-cones and the ridges that connect them. The energy density is highest at the s-cones and is minimum at the ridge's midpoint, half way between adjacent s-cones. The energy density level in the neighborhood of the s-cones is 25 times higher than along
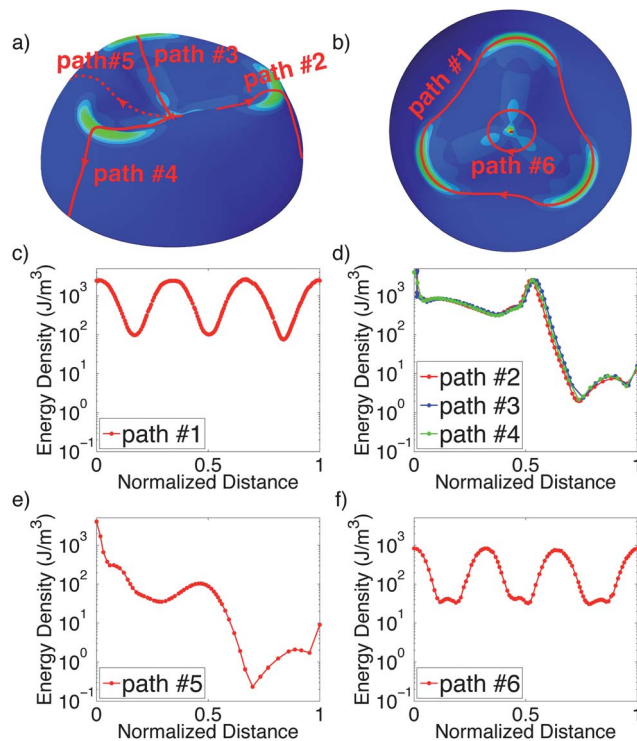

Fig. 3 Energy localization. (a and b) Snapshot from a finite element simulation of a shell indented with a point load. (b) Top view of a shell indented with a point load. (c) Energy density along Path #1, which traces over the three s-cones and the three ridges that connect them. (d) Energy density along Paths #2, #3, and #4 start from the pole of the shell, trace along one of the gullies and one of the s-cones, and end at the base of the shell. (e) Energy density along Path #5, which starts from the pole of the shell, climbs between the s-cones and, traces over the ridge that connects adjacent s-cones, and ends at the base of the shell. (f) Energy density along Path #6, which intersects the three gullies.

the ridges, which is significant of localization. Paths #2, #3, and #4 define meridians; they start from the pole of the shell, pass along a gully, over one of the s-cones, and end at the shell's equator, with each of the paths passing over each of the three s-cones. In Fig. 3d, we plot the energy density along these paths. The maximum of energy occurs at the pole where the indenter contacts the shell. Moving away from the pole, the energy density drops along the gullies, then sharply increases at the s-cones, before rapidly decaying by four orders of magnitude towards zero at the clamped equator of the shell since it is not deformed. The energy density curves corresponding to these three paths are superposed, highlighting the symmetry of the process. In Fig. 3e, we plot the energy density along Path #5, which starts at the pole, traces along one of the faces of the tetrahedron, crosses over the ridge's mid point, and ends at the shell's equator. As stated before, energy is localized most intensely at the pole where the shell is indented. The strain energy along the face of the tetrahedron is small (1% compared to the energy localized at the s-cones). While climbing and traversing over the ridge, there is a small increase in strain energy, indicating that there is some focusing of strain energy at the ridge (4% compared to the energy localized at the s-cones). The energy then decays towards zero at the shell's equator, consistently with the clamping boundary conditions there. In

Fig. 3f, we trace the energy density along Path #6, which is a circular contour near the shell's pole and crosses over the gullies and faces of the tetrahedron. Along this path, the energy is maximum at the gullies. In summary, for point indentation we find that energy is most strongly localized at the s-cones. Energy is localized to less of an extent along gullies and ridges, with energy being focused ten times more along gullies in comparison to ridges.

Varying the shape of the indenter

Having described the behavior observed for point indentation, we now consider the effect of changing the shape of the indenter on the localization process, in both experiments and FEA simulations. The ratio of shell and indenter radii is varied from $\Gamma = 0$ (for point load) to $\Gamma = \infty$ (for plate load), and we consider twelve indenters between these extreme values. In our experiments, we employ rapid prototyping to design and custom fabricate indenters (rigid with respect to the shells) with the range of radii of curvature shown in Fig. 1e. More information on how the indenters are fabricated is given in the Materials and methods section.

In Fig. 4, we present a series of representative experimental and FEA snapshots of the shells, for increasing values of the ratio of shell-to-indenter radii, Γ. In the experimental frames, s-cones are identified by sharp corners in the ridge, as imaged by the white reflection line, and in the FEA simulations they are identified by small regions with a sharp increase in energy density. Localization occurs and s-cones form for all of the indenters, except for $\Gamma = 1, 1.5$ and 2. In the neighborhood of

$\Gamma = 1$, the indenter has a curvature close to that of the shell. As a result, upon indentation their two surfaces remain in complete contact, preventing the formation of s-cones, which would otherwise require delamination from the indenter. We denote this neighborhood of $1 \lesssim \Gamma \lesssim 2$ as the "*localization band gap*", since the formation of s-cones is forbidden for these geometries. The lower bound for the localization band gap is $0.8725 < \Gamma < 1$ (uncertainty of $\sim3\%$) and the upper bound lies in $2 < \Gamma < 2.5$ (uncertainty of $\sim11\%$). This band sets two regions with qualitatively different responses; sharp indenter for $\Gamma \lesssim 1$ and blunt indenters for $\Gamma \gtrsim 2$. Concentrating on the experiments for sharp indenters, the number of s-cones at onset is a minimum ($n = 3$) for point load ($\Gamma = 0$) and it increases with increasing Γ, with the maximum number at onset forming just outside the localization band gap region. For blunt indenters, $n = 5$ s-cones form at onset for plate load ($\Gamma = \infty$), and increasingly more s-cones are observed as Γ is decreased towards $\Gamma \sim 2$. Gullies that connect the s-cones to the pole of the shell form for sharp indenters, but not for blunt indenters.[21] Above, for the case of point load, we saw that past the initial formation of 3 s-cones, a forth can emerge by splitting of a previous one. This mode of transition in the number of s-cones is also observed for other indenter geometries: $n = 4 \rightarrow 5$ for $\Gamma = 0.75$, $n = 6 \rightarrow 7$ for $\Gamma = 10$ and $n = 5 \rightarrow 6 \rightarrow 7$ for $\Gamma = \infty$ (plate load). The FEA simulations show qualitative good agreement with this experimental scenario with differences in the number of s-cones being at most by $n = 1$, possibly due to differences in the details of imperfections between experiments (defects) and FEA (meshing), or a consequence of the fact that multiple states may coexist (as is common in nonlinear systems). Moreover, FEA simulations also exhibit a localization band gap region for $1 \lesssim \Gamma \lesssim 2$ and the same qualitatively different responses for sharp indenters *versus* blunt indenters. In both experiments and FEM (assuming a hyperelastic constitutive model as described in the Materials and methods section), we see that the number of s-cones evolves for $\Gamma > 2$. Previous studies,[21] however, have not seen such an evolution for plate load for the specific case of using a linear elastic model. Establishing whether the discrepancy is due to the material model used or due to the frictional nature of contact that we have considered (both ingredients were used in the FEM to closely reproduce the experiments) is beyond the scope of this paper and will be addressed in a future study.

We have just seen that the geometry of the indenter affects the morphology and number of s-cones at onset. We now proceed by quantifying how the indenter's geometry also sets the critical indentation, δ_c, at the onset of localization, *i.e.* the δ at which the first set of s-cones forms. In Fig. 5, we plot the critical indentation as a function of Γ. As Γ approaches the band gap region in the neighborhood of $\Gamma = 1$, the onset of localization is significantly delayed. The critical indentation exhibits a divergence-like behavior around the band gap region, and the critical indentation is maximum on either side. The critical indentation decreases as $\Gamma \rightarrow 0$ or $\Gamma \rightarrow \infty$ (with the exception of the decrease in δ_c between point load and $\Gamma = 0.5$, which disrupts the otherwise monotonic behavior to the left of the localization band gap). Excellent quantitative agreement is found between experiments and simulations.
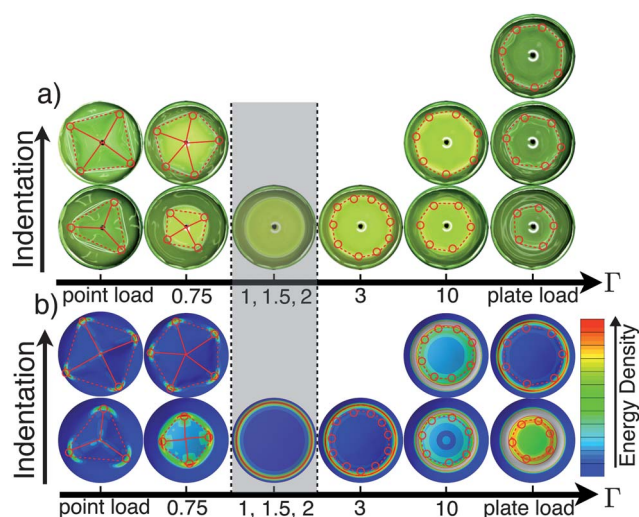

Fig. 4 Varying the shape of the indenters. (a) Snapshots from experiments with elastomeric shells indented at the pole for a variety of indenters, ranging from point load ($\Gamma = 0$) to plate load ($\Gamma = \infty$). (b) The same scenario with the snapshots from the FEA simulations. The color map corresponds to strain energy density. The color and energy scale correspondence is adjusted for each of the images to aid in highlighting localization. Red circles indicate location of s-cones. Dotted red lines are drawn over ridges that connect s-cones along where shell is inverted. Solid red lines are drawn over gullies that connect s-cones to the pole of the shell (only present for $\Gamma < 1$). No localization (indicated by grey area) occurs for indenters with $\Gamma = 1, 1.5,$ or 2.
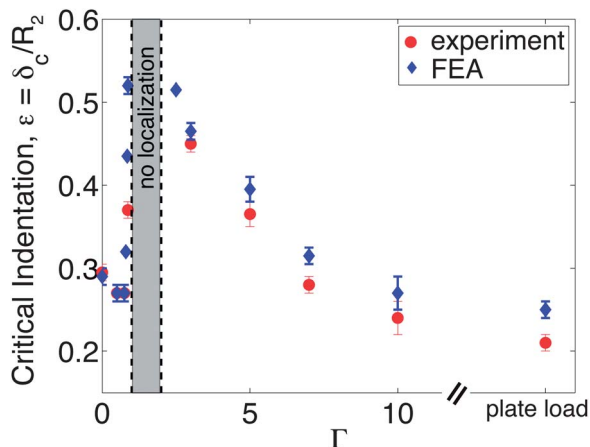
Fig. 5 Critical indentation for the onset of localization *versus* the indenter–shell radii ratio, Γ. No localization occurs between $\Gamma \sim 1$ and $\Gamma \sim 2$ (indicated by the grey region).
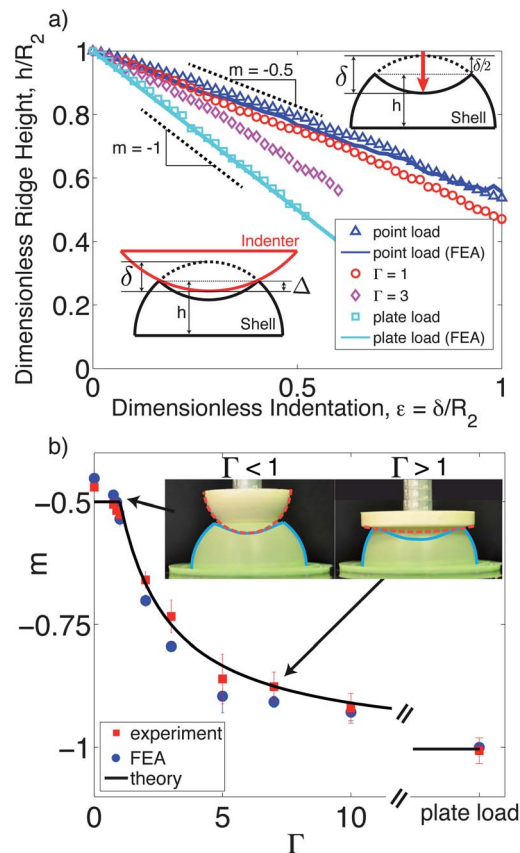

Fig. 6 Ridge-height. (a) Height of the ridge *versus* indentation for indenters with different geometries; experiments (data points) and simulations (solid lines). The schematics on the top right and bottom left corners correspond to the cases of sharp indenters, $\Gamma < 1$, and blunt indenters (indenter in red), $\Gamma > 1$, respectively. (b) Slopes of ridge-height, m vs. indentation curves from experiments (red squares) and simulations (blue circles) indenters ranging from $\Gamma = 0$ to $\Gamma = \infty$. The theory line corresponds to the prediction from eqn (1). Inset illustrates sharp and blunt indenters.

The indenter shape also effects the ridge-height, h, which we define as the vertical distance between the equator of the hemispherical shell, where it is clamped, and the point on the shell at which its surface inverts due to the indentation, thereby forming a ridge. In Fig. 6a, we plot this ridge-height measured experimentally (open symbols), as a function of indentation for point load, $\Gamma = 1$, $\Gamma = 3$, and plate load. For comparison, we superpose the corresponding data from the FEA (solid lines) for the extreme cases of point and plate load. Even for large values of indentation, the ridge-height h decays approximately linearly with indentation, ε. We therefore calculate the slope $m = \mathrm{d}h/\mathrm{d}\delta$, which we plot as a function of the indenter's radii ratio, Γ, in Fig. 6b. The ridge-height decreases the slowest for point indentation, with a rate of $m \sim -0.5$, and the fastest for plate load, with $m \sim -1$ (the ridge moves at the same rate as the indenter). For intermediate indenters ($0 < \Gamma < \infty$) the slope decreases monotonically with Γ and $-0.5 < m < -1$.

We now present a geometric argument that rationalizes these results. The schematic diagram in the top right corner of Fig. 6a illustrates the deformed configuration of the shell for $\Gamma < 1$. Here, the radius of the shell is $R_2 = h + \delta/2$, which in return gives $h/R_2 = 1 - 0.5(\delta/R_2)$ and yields the slope $m = \mathrm{d}h/\mathrm{d}\delta = -0.5$, for $\Gamma < 1$. For $\Gamma > 1$, the nature of contact between the shell and the indenter is qualitatively different, as shown in the schematic diagram in the bottom left corner of Fig. 6a. Taking the radius of the indenter, R_1, into account and assuming small deformations, we obtain $R_2 = h + (\delta - \varDelta)$, where $\varDelta$ is the vertical distance between the pole of the indenter and the ridge-height, h (see schematic in bottom left of Fig. 6b). Using a trigonometric relationship involving R_1, R_2, and a horizontal line constructed between the ridges, we obtain $\varDelta = \delta/(1 + \Gamma)$. Then, $R_2 = h + \delta[1 - 1/(1 + \Gamma)]$ from the geometric construction, which yields the following slope for the h–δ curves,

$$m = \frac{\mathrm{d}h}{\mathrm{d}\delta} = -\left[1 - \frac{1}{1 + \Gamma}\right]. \quad (1)$$

The dependence of m on Γ predicted by this geometric argument underlying eqn (1), which is plotted as the solid line

in Fig. 6b, is in excellent agreement with both the experimental and FEA data. This confirms that the variation in m is due to the different geometric nature of the indenter–shell contact proposed above, and which we explore in more detail next.

In order to achieve the excellent agreement between experiments and simulations highlighted above, we had to treat the shell–indenter interaction with care, and assume a frictional contact, while neglecting adhesion. This is even more important since, as we saw, the nature and morphology of the shell–indenter contact varies for different values of Γ; from sharp indenters to blunt indenters. To stress the important of friction, we now focus on the mechanical response during the indentation process, as quantified by the indentation load, P, as a function of indentation, ε. A series of P–ε curves for increasing values of Γ is presented in Fig. 7a. For small indentation, there is a linear regime significant of the shell's stiffness, as previously described by ref. 12 and 31. For large indentations, all curves with $\Gamma < 1$ eventually asymptote to an approximately constant value. In contrast, the various curves with $\Gamma > 1$ exhibit an inflection point and fan out; higher values of Γ result in higher loads. Again, we observe a quantitative difference
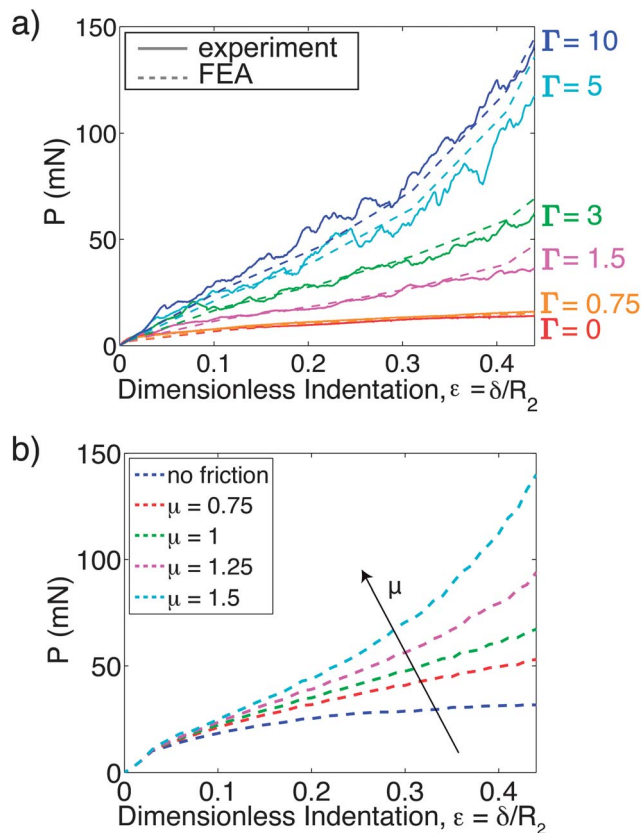
Fig. 7 Mechanical response and the effect of friction. (a) Force–indentation curves from experiments (solid lines) and finite element simulations (dashed lines) for a variety of indenters. Coefficients of friction for Γ = 0, 0.75, 1.5, 3, 5, 10 are, respectively, μ = 0, 1.5, 1.2, 1.2, 1.7, 1.5. (b) Force–indentation curves from simulations for Γ = 10 for no friction and a variety of friction coefficients.

between sharp and blunt indenters. For $\Gamma > 1$, a significantly higher load is required to indent a shell when compared with sharp indenters ($\Gamma < 1$) due to the different nature of the indenter–shell contact. For sharp indenters, the poles of the indenters and the shells remain in contact throughout indentation. On the other hand, for blunt indenters, the shell delaminates from the pole of the indenter, and pushes onto the shell at its ridges. This requires a substantially higher force level (as high as a factor of 10 for $\varepsilon = 0.4$, when comparing $\Gamma = 0$ and $\Gamma = 10$) and also involves sliding and rolling of the two surfaces. These two scenarios are illustrated in the inset of Fig. 6b.

From the detailed comparison between the experimental and FEA force–indentation curves, we have learned that friction plays an essential role on the mechanical response. Force–indentation curves from simulations without friction showed a much lower mechanical response than what was measured experimentally. As presented in Fig. 7b, when the coefficient of friction μ is increased, the load required to indent the shell is also significantly increased. For example, at $\varepsilon = 0.45$, the load required to indent a shell for $\mu = 1.5$ is increased by a factor as large as 5, when compared to doing so for a frictionless indenter–shell contact. Using an independent friction sliding test (details in Materials and methods), the friction coefficient was experimentally measured to be $\mu = 1.46 \pm 0.53$. The large

variation in this measured value can be attributed to the fact that a dry friction description is oversimplistic for polymer–polymer surface contacts. Still, in the FEA, we have treated μ as a fitting parameter, bound within the measured experimental range. This is appropriate since the experimental friction coefficients for each of the individual indenters are not precisely known due to the varying levels of roughness for indenters of different curvature, imparted by the fabrication process and set by the resolution of the CNC milling process.

Discussion and conclusion

Without a general predictive analytical model of the localization process at hand, we are lead to speculate that geometric frustration underpins the buckling transition from the axisymmetric state into the onset of s-cones. We believe that the mechanism is related to that recently reported by Dias et al.,[32] who studied the mechanics of folding of an annular flat plate containing a concentric circular crease. Folding the crease induces out-of-plane buckling of the plate. Further increasing the dihedral angle of the fold, results in increasingly more nonplanar configurations and an increasing storage of stretching energy at the crease. Geometric and topological constraints, coupled with the mechanics of plates, dictate the permissible configurations. Similarly in our system, indentation introduces geometric frustration that disrupts the isometry of the shell's inverted cap. Once the circular ridge forms, the angle of the folded region where curvature of the shell inverts, increases as the shell is indented further which leads to a growing storage of strain energy at the ridge (the angle can be derived using an argument similar to that presented for the slope of the ridge-height vs. indentation curves). Past a critical indentation (quantified in Fig. 5) the circular ridge looses symmetry and stretching, due to its high energetic cost, is focused onto localized structures, the s-cones.

We now comment on the observation that the number of s-cones at onset increases, when the curvature of the indenter approaches the shell's curvature. For this, we establish an analogy with buckling of confined elastica. When a slender beam is compressed axially, but its transverse displacement is constrained by two confining walls,[33,34] high-order buckling modes can be excited (in contrast to the classic mode-one Euler buckling when the beam is unconstrained). In this case, the buckling wavelength increases with the lateral confinement and the geometric constraint of the two confining walls is the driving mechanism for exciting high-order buckling modes. Following this analogy, point load indentation in our problem can be considered as being unconstrained. At the other extreme, when $\Gamma \sim 1$, the surfaces of the shell and indenter are in close contact with each other, preventing the shell from delaminating from the indenter, thereby precluding local buckling (no s-cones form). In the constrained Euler buckling analogy, this corresponds to the case where the two constraining plates are separated by a distance equal to the thickness of the strip such that buckling cannot occur. For $\Gamma > 0$, and outside the localization band gap in the neighborhood of $\Gamma \sim 1$, however, the shell–indenter contact constrains the buckling morphology,

which excites higher order modes (increasing the number of s-cones) and affecting the onset of localization.

In conclusion, we have presented a rich scenario for the large deformation of a thin shell under indentation, as the curvature of the indenter is systematically varied, which has a strong effect on the onset and evolution of localized structures. The nature of the contact between the shell and the indenter was found to be a crucial ingredient to the process; friction between the indenter and the shell significantly affects the shells's load-bearing capacity, especially for blunt indenters ($\Gamma > 1$), which require significantly higher loads to indent shells compared to sharp indenters ($\Gamma < 1$). The robustness of the observed localization behavior and the excellent agreement found between experiments and numerics suggest that there is an underlying mechanism at play that arises from the strong interplay between geometry and mechanics. We hope that our exploratory study will help catalyze further theoretical efforts in this direction. Moreover, given the scale-invariance of the scenario presented here, our results should find uses at the microscale for AFM, where it is crucial to understand how the curvature of the tip, relative to the object being indented, affects the mechanical response.

Materials and methods

Experiments

The shells and the indenters are fabricated using rapid prototyping. Starting from a computer assisted design, a model of a mold was created with the targeted shell or indenter geometry. Molds were then machined from polyacetal with a CNC milling machine. Shells were fabricated with a coating technique (Fig. 1a). Vinylpolysiloxane (a silicone based elastomer) was used to make the shells. VPS has a shear modulus $G_0 = 454.6$ kPa, a Poisson ratio of $\nu = 0.5$, and the neo-Hookean strain energy potential coefficients of $C_{10} = 227\,300$ Pa, and $D_1 = 2.36 \times 10^{-8}$ Pa^{-1}. The polymer was poured into a mold, which was then rotated so that the polymer wetted the entire surface of the mold. Then, the excess was poured out and the mold was left upside-down to allow the excess to drain out while the polymer cures. The resulting shells had a radius of $R_2 = 25$ mm and a thickness of $t = 0.280 \pm 0.027$ mm, which is set by a combination of the viscosity of the polymer and the length of the curing time. In a scenario similar to Landau–Levich dip coating for fibers and plates,[35] this fabrication method creates shells with small variations on their thickness ($\sim$9.7%).

Indenter fabrication. Twelve indenters were designed with a variety of radii of curvature so that the ratio of the radius of the indenter and the radius of the shell, $\Gamma = R_1/R_2$ had the following values: $\Gamma = 0$ (point load), 0.5, 0.75, 0.8725, 1, 1.5, 2, 3, 5, 7, 10, and ∞ (plate load) (Fig. 1e). Indenters with Γ ranging from 0.5 to 10 were cast with a hard polyurethane. The indenter for point load was a steel screw with a hemispherical cap (1.5 mm radius). The indenter for plate load was cut from a sheet of acrylic. All indenters can be considered rigid relative to the elastomeric shells. The polyurethane used to cast the indenters has a Young's modulus $E = 147$ MPa and the vinylpolysiloxane used to cast the shells has a Young's modulus $E = 1.36$ MPa.

Mechanical testing. Shells are indented at the pole using the fabricated indenters at a constant speed of 5 mm.min^{-1}. The compressive force, F, from the indentation by the imposed displacement, δ, is recorded using the load cell of an Instron machine with a resolution of ± 100 μN. The evolution of the deformation of the shell is recorded with digital images that are captured from underneath the shells.

Friction tests. The friction from the contact between the shell and the indenter was measured through friction tests. A block of vinylpolysiloxane (the shell material) with a force sensor attached was pulled horizontally along a surface made of polyurethane (the indenter material). The coefficient of friction, measured as the average from ten experiments of the ratio of the force required to pull the block to the weight of the block, was measured to be $\mu = 1.46 \pm 0.53$.

Numerical simulations

Numerical simulations were performed using the commercial finite element package ABAQUS/CAE (SIMULIA, Providence, RI). One half of the 3D spherical shell was modeled with a clamped boundary condition on the free edge, indenters were modeled as analytical rigid shells with a displacement-control boundary condition. For the material properties, we used an isotropic hyperelastic model using the material parameters measured independently in the experiments. Four-node thin shell elements with reduced integration (element type S4R) were used in all simulations and a mesh sensitivity study was carried out to ensure that the results are minimally sensitive to the element size. We used the free mesh scheme available in Abaqus and no initial geometric or material imperfection was included in the computational model. To capture the local instabilities in the structure, we used a stabilizing mechanism (available in Abaqus/Standard solver) based on automatic addition of volume-proportional damping, which was decreased systematically to ensure that the response was insensitive to this change. To model friction, a penalty formulation was used with the appropriate coefficient.

Acknowledgements

References

1 S. S. Datta, S.-H. Kim, J. Paulose, A. Abbaspourrad, D. R. Nelson and D. A. Weitz, *Phys. Rev. Lett.*, 2012, **109**, 134302.

2 X. Zhang, *Proc. Inst. Mech. Eng., Part G*, 1998, **212**, 245–259.

3 W. Johnson and A. Mamalis, *Crashworthiness of vehicles*, Mechanical Engineering Publications Limited, 1978.

4 B. Mercatoris and T. Massart, *Int. J. Numer. Meth. Eng.*, 2011, **85**, 1177–1206.

5 J. Zessin, W. Lau and J. Ochsendorf, *Proceedings of the ICE – Engineering and Computational Mechanics*, 2010, **163**, 135–145.

6   K. Costa, F. Yin, *et al.*, *J. Biomech. Eng.*, 1999, **121**, 462.

7   F. Dubreuil, N. Elsner and A. Fery, *Eur. Phys. J. E: Soft Matter Biol. Phys.*, 2003, **12**, 215–221.

8   M. Arnoldi, M. Fritz, E. Bäuerlein, M. Radmacher, E. Sackmann and A. Boulbitch, *Phys. Rev. E: Stat. Phys., Plasmas, Fluids, Relat. Interdiscip. Top.*, 2000, **62**, 1034–1044.

9   S. Timoshenko, S. Woinowsky-Krieger and S. Woinowsky, *Theory of plates and shells*, McGraw-Hill, New York, 1959, vol. 2.

10 A. Vaziri and L. Mahadevan, *Proc. Natl. Acad. Sci. U. S. A.*, 2008, **105**, 7913–7918.

11 E. Reissner, *J. Math. Phys.*, 1946, **25**, 80.

12 A. Lazarus, H. C. B. Florijn and P. M. Reis, *Phys. Rev. Lett.*, 2012, **109**, 144301.

13 T. Witten, *Rev. Mod. Phys.*, 2007, **79**, 643.

14 A. Lobkovsky, S. Gentges, H. Li, D. Morse and T. Witten, *Science*, 1995, **270**, 1482–1485.

15 A. Lobkovsky and T. Witten, *Phys. Rev. E: Stat. Phys., Plasmas, Fluids, Relat. Interdiscip. Top.*, 1997, **55**, 1577.

16 A. E. Lobkovsky, *Phys. Rev. E: Stat. Phys., Plasmas, Fluids, Relat. Interdiscip. Top.*, 1996, **53**, 3750–3759.

17 E. Hamm, B. Roman and F. Melo, *Phys. Rev. E: Stat., Nonlinear, Soft Matter Phys.*, 2004, **70**, 026607.

18 S. Knoche and J. Kierfeld, *Phys. Rev. E: Stat., Nonlinear, Soft Matter Phys.*, 2011, **84**, 046608.

19 C. Quilliet, *Eur. Phys. J. E: Soft Matter Biol. Phys.*, 2012, **35**, 9725.

20 C. Quilliet, C. Zoldesi, C. Riera, A. Van Blaaderen and A. Imhof, *Eur. Phys. J. E: Soft Matter Biol. Phys.*, 2008, **27**, 13–20.

21 A. Vaziri, *Thin Wall. Struct.*, 2009, **47**, 692–700.

22 S. N. Amiri and H. A. Rasheed, *Thin Wall. Struct.*, 2012, **53**, 72–82.

23 H. Ruan, Z. Gao and T. Yu, *Int. J. Mech. Sci.*, 2006, **48**, 117–133.

24 D. P. Updike and A. Kalnins, *J. Appl. Mech.*, 1972, **39**, 1110–1114.

25 D. P. Updike and A. Kalnins, *J. Appl. Mech.*, 1970, **37**, 635–640.

26 L. Pauchard, Y. Pomeau and S. Rica, *C. R. Mec.*, 1997, **324**, 411–418.

27 X. Dong, Z. Gao and T. Yu, *Int. J. Impact Eng.*, 2008, **35**, 717–726.

28 N. Gupta, G. Easwara Prasad and S. Gupta, *Thin Wall. Struct.*, 1999, **34**, 21–41.

29 R. Kitching, R. Houlston and W. Johnson, *Int. J. Mech. Sci.*, 1975, **17**, 693–703.

30 A. Pogorelov, *Bendings of surfaces and stability of shells*, American Mathematical Society, 1988, vol. 72.

31 D. Vella, A. Ajdari, A. Vaziri and A. Boudaoud, *Phys. Rev. Lett.*, 2012, **109**, 144302.

32 M. A. Dias, L. H. Dudte, L. Mahadevan and C. D. Santangelo, *Phys. Rev. Lett.*, 2012, **109**, 114301.

33 A. Pocheau and B. Roman, *Physica D*, 2004, **192**, 161–186.

34 B. Roman and A. Pocheau, *J. Mech. Phys. Solids*, 2002, **50**, 2379–2401.

35 L. Landau and B. Levich, *Acta Physicochim. URSS*, 1942, **17**, 42–54.